UC Irvine
UC Irvine Previously Published Works

Title

Measurements of fast-ion acceleration at cyclotron harmonics using Balmer-alpha spectroscopy

Permalink

https://escholarship.org/uc/item/9c48h40w

Journal

Plasma Physics and Controlled Fusion, 49(9)

ISSN

0741-3335

Authors

Heidbrink, WW
Luo, Y
Burrell, KH
et al.

Publication Date

2007-09-01

DOI

10.1088/0741-3335/49/9/008

Copyright Information

Peer reviewed

Measurements of fast-ion acceleration at cyclotron harmonics using Balmer-alpha spectroscopy

W W Heidbrink[1], Y Luo[1], K H Burrell[2], R W Harvey[3], R I Pinsker[2] and E Ruskov[1]

[1] University of California, Irvine, California, USA
[2] General Atomics, San Diego, California, USA
[3] CompX, Del Mar, California, USA

Abstract

Combined neutral beam injection and fast wave heating at the fourth and fifth cyclotron harmonics accelerate fast ions in the DIII-D tokamak. Measurements with a nine-channel fast-ion D-alpha (FIDA) diagnostic indicate the formation of a fast-ion tail above the injection energy. Tail formation correlates with enhancement of the d–d neutron rate above the value that is expected in the absence of fast-wave acceleration. FIDA spatial profiles and fast-ion pressure profiles inferred from the equilibrium both indicate that the acceleration is near the magnetic axis for a centrally located resonance layer. The enhancement is largest 8–10 cm beyond the radius where the wave frequency equals the cyclotron harmonic, probably due to a combination of Doppler-shift and orbital effects. The fast-ion distribution function calculated by the CQL3D Fokker–Planck code is fairly consistent with the data.

(Some figures in this article are in colour only in the electronic version)

1. Introduction

Cyclotron damping of fast waves in the ion cyclotron range of frequencies is a standard heating scheme in magnetic fusion devices. Injected beam ions have been accelerated by ion cyclotron heating (ICH) at cyclotron harmonics in many tokamaks [1–17]. Most measurements of acceleration by ICH have employed neutral particle analysis [18, 19], although fusion reaction measurements of neutrons and charged fusion products are also common [19, 20]. Differences between the perpendicular and equilibrium stored energy are used to measure the anisotropic fast-ion energy [21]. Measurements of fast ions that escape on loss orbits can also diagnose ion acceleration [22]. In recent years, gamma-ray tomography has emerged as a powerful technique [23, 24]. Collective Thomson scattering has also detected ions accelerated by ICH [25].

Deuterium beam-ion acceleration at the 4th–8th harmonics was previously studied on the DIII-D tokamak using established techniques [8, 10, 11, 14, 26, 27]. Recently, a new fast-ion diagnostic technique was demonstrated at DIII-D during neutral beam injection [28]. Fast ions that charge exchange with an injected neutral beam can emit Doppler-shifted Balmer-alpha light. A dedicated instrument [29] that was designed to measure this fast-ion D-alpha (FIDA) light achieved a spatial resolution of a few centimeters, an energy resolution of ~ 10 keV, and a temporal resolution of 1 ms [30]. For a vertical viewing geometry, the photon Doppler shift is proportional to the vertical component of the fast-ion velocity, so measurements with this instrument are sensitive to perpendicular acceleration. This paper contains the first measurements of ion cyclotron acceleration using FIDA spectroscopy.

Section 2.1 describes the plasma conditions and fast-ion diagnostics, including a detailed discussion of the portion of velocity space measured by FIDA spectroscopy. Section 2.2 contains examples of FIDA spectra and profiles. A database of fast-ion signals confirms the validity of the FIDA measurements (section 2.3). Comparisons of the FIDA spectra and profiles with predictions based on calculations by the CQL3D [31] Fokker–Planck code show reasonable agreement (section 3). Section 4 states the major conclusion of the paper: FIDA spectroscopy is a powerful technique for measurement of the energy spectrum and spatial profile of ICH. Additional diagnostic details appear in the appendix.

2. Data

2.1. Plasma and fast-ion diagnostics

The experiments were performed in the DIII-D tokamak (major radius $R_0 \simeq 1.7$ m, minor radius $a \simeq 0.6$ m, graphite walls, deuterium plasmas) at the end of the 2005 campaign. The conditions are nearly identical to the ones reported in [11]. Typically, one transmitter couples 0.7–1.0 MW at 60 MHz into L-mode plasmas. Counter-current drive phasing (90° toroidal phasing between straps) is employed, with the peak in the vacuum spectrum at $n_\parallel \simeq 5$. In some discharges, other transmitters couple up to 2 MW of power at 113–117 MHz but these waves have little effect on the fast ions [32] and are not discussed here. At the usual toroidal field of 1.9 T, the 60 MHz waves resonate with the deuterium cyclotron harmonic at several radial locations, with the central resonance corresponding to the fourth harmonic (figure 1(*a*)). The beams inject 75–81 keV deuterium beam ions in the direction of the plasma current at tangency radii of 0.76 m (for the so-called 'right' sources) and 1.15 m (for the 'left' sources) (figure 1(*b*)). Most plasmas are upper single null divertor discharges with an elongation of $\kappa = 1.7$. The ∇B drift is usually downward to avoid H-mode transitions. Spectroscopic measurements of the cold H-alpha and D-alpha lines imply that the hydrogen concentration is usually below 1%. The dominant impurity is carbon and charge-exchange recombination [33] measurements indicate typical central ion temperatures of $T_i = 5$ keV, toroidal rotation velocities of 2×10^7 cm s^{-1}, and impurity concentrations of $Z_{\text{eff}} = 1.5$.

A plastic scintillator that is cross-calibrated to an absolutely calibrated fission counter measures the volume-averaged 2.5 MeV neutron rate [34]. Spatially resolved measurements of the fast ions are obtained three ways. A compact electrostatic neutral particle analyser (NPA) measures the active charge exchange signal at $R = 1.95$ m [35]; the analyser detects perpendicular 50 keV neutrals from a vertical volume that is determined by the vertical extent of the modulated neutral beam (figure 1). The second spatially resolved diagnostic relies on motional Stark effect (MSE) [36] measurements of the internal magnetic field. The profile of the total plasma pressure p_{tot} is obtained from EFIT [37] reconstructions of the MHD equilibrium that are consistent with the MSE data, with magnetics data, and with isotherms of
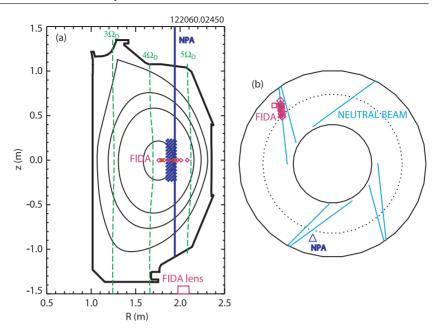
Figure 1. (*a*) Elevation of the DIII-D vacuum vessel, showing the separatrix and the $q = 1, 2$ and 3 surfaces (solid black curves), the locations where ω_{RF} equals the third, fourth and fifth deuterium cyclotron harmonic (dashed green curves), the NPA sightline (thick blue vertical line), and the midplane locations of the FIDA Reticon (diamond) and CCD (solid triangle) chords. The hashed region represents the approximate vertical extent of the heating beam that produces the FIDA and NPA signals. The square indicates the approximate location of the FIDA collection optics. (*b*) Plan view of the vessel, showing the toroidal location of the FIDA and NPA diagnostics and the centerlines of the various left and right beams. The dotted line represents the magnetic axis.

the electron temperature as measured by an electron cyclotron emission (ECE) [38] diagnostic. The thermal pressure p_{th} from T_e [38, 39], n_e [39, 40], T_i and carbon density measurements is subtracted from the MHD pressure profile to obtain the fast-ion pressure profile p_f [8, 11]. The uncertainty in p_f is affected by both the uncertainty in the total pressure and the uncertainty in thermal pressure. The uncertainty in p_{th} is readily computed by propagating the estimated random errors in the thermal density and temperature measurements. The uncertainty in p_{tot} is more difficult to quantify because systematic errors in the EFIT equilibrium construction exceed the errors associated with MSE, ECE, and magnetics measurement errors. For the cases shown here, the absolute uncertainty in the fast-ion pressure is $\sim 20\%$ (with δp_{tot} and δn_e making the dominant contributions), while the relative uncertainty when comparing the profiles with and without ICH is $\sim 10\%$.

The fourth and primary fast-ion diagnostic is FIDA. Beam modulation and fitting of impurity lines is used to extract the fast-ion spectra from the interfering background light [30]; uncertainties in background subtraction are the dominant source of error and are represented by error bars in the figures. In this paper, the spectra are often averaged over wavelength for improved statistics. The wavelength bin is specified in terms of energy E_λ along the (nearly vertical) viewing chord. In reality, since the photon Doppler shift is only determined by one component of the velocity, the diagnostic performs an effective average in velocity space over this and higher energies [30, 41]. Since the signals are proportional to the product of the injected neutral density and the fast-ion density, the wavelength-integrated signals are usually divided

by the injected neutral density (as calculated by a pencil-beam code) to yield fast-ion 'density' measurements over the high-energy portion of velocity space. Two different instruments are employed. One of these [29] measures spectra at two spatial locations with a high quantum efficiency CCD camera. The second instrument has seven spatial channels but only measures a portion of the spectrum (on the blue-shifted side) with slower, noisier Reticon photodiode detectors. The spatial locations of the nine spatial channels are illustrated in figure 1. In MHD-quiescent plasmas, the absolute magnitude of the spectra from the CCD channels is in excellent agreement with simulations that employ the TRANSP [42] fast-ion distribution function but the absolute profile for the Reticon detectors is inconsistent with theory [43]. In contrast, relative changes in spatial profile are in excellent agreement with theory for both systems [43]. Accordingly, in this paper, all spatial profiles are relative comparisons of the profile without ICH to the profile with ICH. Unless otherwise indicated, the FIDA data in this paper are from the dedicated system.

Balmer-alpha light can be emitted by hydrogen atoms as well as deuterium atoms. For central fourth-harmonic heating on the deuterium beam ions, parasitic absorption by hydrogen at the second harmonic also occurs. Although the residual hydrogen density in these experiments is quite low (edge spectroscopy indicates that the hydrogen to deuterium concentration is $< 1\%$), a dilute population of hydrogen fast ions probably exists that contributes to the FIDA signal. Empirically, there is no evidence of contamination of the spectrum by hydrogen. Estimates based on calculations of the parasitic hydrogen absorption [11] indicate that hydrogen fast ions may contribute $\lesssim 5\%$ of the signal at $E_\lambda > 50\,\text{keV}$ during fourth harmonic heating. During fifth harmonic heating, any contribution is negligible.

The different fast-ion diagnostics weight the fast-ion distribution function differently in velocity space (figure 2). Because of the rapid gyromotion, two velocity-space coordinates suffice to describe the fast-ion distribution function. In this work, the fast-ion energy E and the pitch $p = v_\parallel/v$ are the selected coordinates. Figure 2(a) shows the fast-ion distribution function calculated by TRANSP, $F(E, p)$, at the location of the $R = 180\,\text{cm}$ FIDA channel for a typical discharge in this study. (The definition of F employed by TRANSP includes the Jacobian so that $\int\int F(E, p)\,\mathrm{d}E\,\mathrm{d}p$ yields the fast-ion density.) For injection by the more-tangential left beams, the distribution peaks near $p \simeq 0.6$ in the plasma center. The NPA has excellent energy resolution ($\sim 3\%$) and is narrowly collimated ($\sim 1°$), so the NPA essentially measures a point in velocity space (figure 2(a)). It is convenient to describe the velocity-space weighting of the various diagnostics by a weight function, $W(E, p)$. The signal from the diagnostic is then $S = \int\int W(E, p)F(E, p)\,\mathrm{d}E\,\mathrm{d}p$. For the NPA, W is nearly a delta function at $E = 50\,\text{keV}$ and $p = 0$. As a result, the signal (figure 2(b)) comes from the same portion of velocity space as the peak in the weight function.

The weight function W for FIDA (figure 2(c)) depends on several factors. Through the photon Doppler shift, a particular wavelength corresponds to a vertical energy E_λ. Once a value of E_λ is specified, the minimum energy that can contribute this vertical energy consists of a curve in velocity space [30]. For a vertical view, this curve is $E = E_\lambda/(1 - p^2)$; this accounts for the approximately parabolic shape of the $W \neq 0$ region in figure 2(c). Within this region, the probability of emitting a photon with the specified wavelength is largest for ions near the minimum-energy boundary (because they spend a greater fraction of their gyromotion heading in the desired direction). This effect is symmetric in pitch and explains why the weight function peaks at the minimum-energy curve. The final effect is associated with the probability of a charge-exchange reaction. Reactions are more probable for fast ions that have a component of velocity in the direction of the injected neutral beam; the weight function is skewed toward positive values of pitch by this effect. Weight functions for other values of E_λ are qualitatively similar (not shown). As figure 2(d) shows, for a typical distribution function,
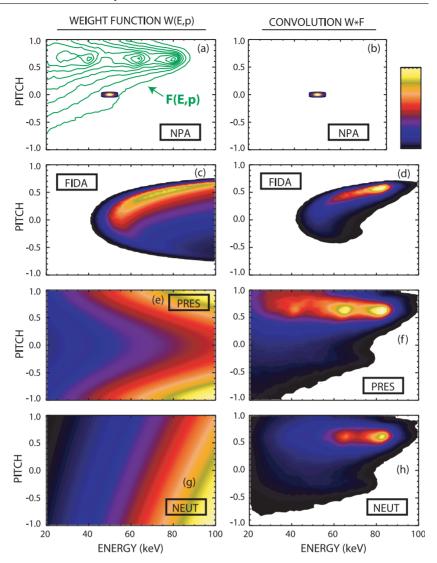
Figure 2. Contour plots of the velocity-space weight functions (left column) for the NPA, FIDA, p_f, and neutron diagnostics for discharge #122060 before the ICH. The bar graph in the upper right figure shows the linear color scale in normalized units. The upper left graph also shows the fast-ion distribution function $F(E, p)$ calculated by TRANSP at the location of the 180 cm FIDA channel. The right column shows contour plots of the product of the weight function with the TRANSP distribution function for the four fast-ion diagnostics. The FIDA graphs use the calculated injected neutral densities at 180 cm (full : half : third of 57% : 26% : 17%), include an approximate treatment of the instrumental resolution (Gaussian spread with $\sigma = 0.21$ nm), and assume $E_\lambda = 50$ keV. The neutron weight function is for beam-plasma reactions only and employs the measured ion temperature (5.0 keV) and toroidal rotation (2.1×10^7 cm s^{-1}). The weight function is negligible in the white regions.

the FIDA signal for $E_\lambda = 50$ keV is actually dominated by ions born near the injection energy and angle ($E \simeq 80$ keV; $p \simeq 0.6$).

The weight function W for the fast-ion pressure measurement extends throughout velocity space (figure 2(e)). Each ion contributes $E_\parallel + \frac{1}{2}E_\perp$ to the MHD pressure, so the weight function

is larger for large $|p|$ than for small $|p|$. Convolution with a typical distribution function shows that the pressure measurement samples much of the distribution function, with the greatest contribution from full-energy beam ions (figure 2(f)).

In these plasmas, the neutron rate is dominated by beam-plasma reactions. (TRANSP computes that $\sim 80\%$ of the reactions are from beam-plasma, while most of the remainder are from beam-beam reactions.) Figure 2(g) shows the weight function for beam-plasma reactions. The weight increases rapidly with energy because the d–d fusion cross section increases rapidly with energy. The asymmetry in pitch is associated with plasma rotation: for a given fast-ion energy, the reaction probability is higher for a counter-going ion because the relative velocity between the fast ion and the thermal ions is larger. Because of the strong energy weighting, the neutron signal arises primarily from fast ions near the injection energy (figure 2(h)).

Comparison of the figures (right-hand column in figure 2) shows that, despite the substantial differences between the FIDA, pressure, and neutron measurements, the signals actually arise from the same region in velocity space. The NPA diagnostic is unique in sampling a region of the distribution far from the bulk. Of course, there is also an important distinction between diagnostics in configuration space: the NPA, FIDA, and pressure diagnostics are local measurements, while the neutron diagnostic is volume-averaged.

Additional details of the uncertainty analysis and weight function calculations appear in the appendix.

2.2. FIDA measurements

The temporal evolution of a discharge with central fourth harmonic heating is shown in figure 3. Neutral beam injection commences 0.6 s after the current reaches its flat top value of 1.0 MA. To accommodate the diagnostics, five modulated sources inject into the plasma but the average total power is 3.6 MW. The total power only varies for 10 ms, which is much less than the beam ion slowing down time of $\tau_s \simeq 100$ ms. The 60 MHz system couples ~ 1 MW of power between 2.2 and 3.7 s. At 3.3 s, the neutral beam injection switches from the more tangential left sources to the more perpendicular right sources. With the application of RF power, the neutron rate increases on a τ_s timescale. The central electron temperature increases and the sawtooth period increases during ICH but transient periods of sawtooth stabilization ('monster' sawteeth [44]) are not observed. Analysis of magnetics and far-infrared scattering [45] signals shows that Alfvén modes are weak or absent in this discharge.

During the ICH, the neutron rate increases more than classically predicted (figure 3(c)), indicating acceleration of energetic ions by the 60 MHz waves. The central FIDA data (figure 3(d)) show that the acceleration is greatest for energies near or above the injection energy. Evidently, the slope of the energy distribution is distorted by the harmonic heating.

Comparison of the FIDA spectra before and during ICH (figure 4) clearly shows that fast ions are accelerated above the injection energy. Prior to ICH, the spectra are in good agreement in magnitude and shape with the spectra predicted by a FIDA simulation code [28, 43] that uses the distribution function from collisional processes (as predicted by TRANSP) and includes all relevant atomic physics effects. In the absence of RF acceleration, the predicted spectra are only expected to change slightly in the latter phase of the discharge but the observed increase is much larger, owing to the ion cyclotron acceleration. The distortion in the measured slope begins at a wavelength that corresponds to $E_\lambda \simeq 50$ keV. Because fourth harmonic heating is a finite Larmor radius effect that depends upon the value of $k_\perp \rho_f$, this is consistent with the theoretical expectation that higher energy ions should be most strongly affected. (Here $k_\perp$ is the perpendicular wavenumber and ρ_f is the fast-ion gyroradius.)
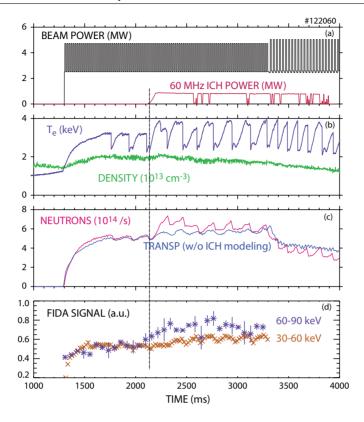
Figure 3. Time evolution of (*a*) the injected neutral beam and coupled ICH power, (*b*) the central electron temperature and the line-average electron density, (c) the measured neutron rate and the classically expected rate in the absence of ion cyclotron acceleration and (*d*) the FIDA signal in two spectral bands. The more tangential left beams are injected from 1300 to 3300 ms, while more perpendicular right beams are injected after 3300 ms. For the FIDA data, the '30–60 keV' signal represents E_λ between 30 and 60 keV (wavelengths between 650.8–652.4 and 659.8–661.3 nm) and the '60–90 keV' signal integrates wavelengths between 649.6–650.8 and 661.3–662.6 nm. The radial position of the FIDA channel is centered at $R = 195.4$ cm. $B_T = 1.92$ T; $I_p = 1.0$ MA.

Strong acceleration is also sometimes observed at lower toroidal field when the fifth harmonic layer is near the magnetic axis. Figure 5 shows the time evolution of a low-power discharge with particularly large acceleration. The average beam power is only 1.2 MW and the coupled ICH power is 0.8 MW in this case (figure 5(*a*)). The electron density and temperature are both relatively low (figure 5(*b*)). With the onset of ICH, the neutron rate nearly doubles (figure 5(*c*)), presumably because the power per particle is large. Because the number of fast ions is relatively low, the NPA and FIDA signals have rather poor statistics (figures 5(*d*) and (*e*)) but a significant increase is observed by both diagnostics during ICH. The angle of beam injection switches from exclusively Left to primarily Right sources midway through the ICH pulse (at 2.75 s). This causes a large jump in NPA signal that is classically expected and that persists after the RF. The vertically viewing NPA only detects perpendicular ions, so ions injected by the right source need only pitch-angle scatter $\sim 23°$ to be detected, while ions from the left source must scatter $\sim 36°$. In contrast, because they arise from effective averages over pitch angle in velocity space, the FIDA and neutron signals hardly change when the injection angle changes.
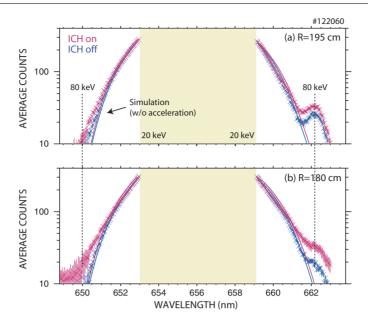
Figure 4. Average FIDA spectra (symbols) with and without ICH for the channels at (*a*) $R = 195$ cm and (*b*) 180 cm in the discharge shown in figure 3 between 2250–2500 ms and 1700–2000 ms, respectively. The solid lines show the spectra predicted by the FIDA simulation code for the TRANSP fast-ion distribution function calculated in the absence of ICH acceleration. The dotted vertical lines indicate the wavelengths that correspond to $E_\lambda = 80$ keV. The FIDA simulation only treated the portion of the fast-ion distribution function with energies above 20 keV. Although the most prominent impurity lines have already been fitted and removed from the spectra [30], an impurity line at 662.15 nm still appears.

Measurements of the spatial profile are shown in figure 6. Consider first the fourth-harmonic discharge shown in figure 3. In the absence of RF acceleration, very little change in fast-ion pressure is expected during ICH (figure 6(*a*)). (The increase in T_e is modest so the slowing-down time barely increases.) Before RF, the measured p_f profile agrees with the TRANSP prediction within estimated experimental error. With ICH, the pressure profile increases significantly in the center of the discharge. For comparison, the relative change in the FIDA density profile is plotted on the same graph using the before-ICH profile as normalization. It should be noted that, because of different weighting in velocity space (figure 2), the p_f and the FIDA profiles need not be identical, although the difference in relative shape is expected to be small in these conditions. In light of the differences between the quantities, the agreement is excellent.

Figure 6(*b*) shows spatial profiles in a high density, fourth-harmonic discharge that had very little enhancement in the neutron rate [32]. As before, in the absence of RF acceleration, no significant difference in p_f is expected in the ICH and no-ICH phases but, in this case, the fast-ion pressure profile inferred from the equilibrium hardly changes as well. The FIDA profile (not shown) also hardly changes but has large error bars because of the high density.

The spatial profiles for the fifth-harmonic discharge shown in figure 5 appear in figure 6(*c*). Here, as in the other cases, little change in pressure profile is expected between the ICH and no-ICH phases in the absence of RF acceleration. However, in this case, the measured pressure profile prior to the RF is broader than predicted classically. A likely cause of this broadening is the larger sawteeth in this lower toroidal field, lower q discharge. (The $q = 1$ surface is at
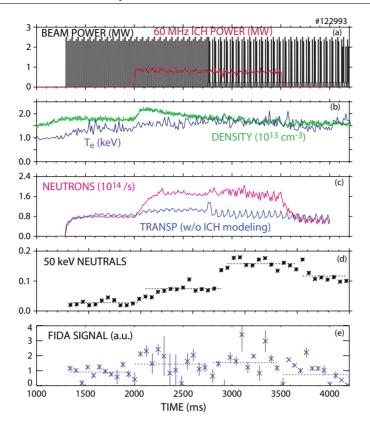
Figure 5. Time evolution of (*a*) the injected neutral beam and coupled ICH power, (*b*) the central electron temperature and the line-average electron density, (*c*) the measured neutron rate and the classically expected rate in the absence of ion cyclotron acceleration, (*d*) the active charge-exchange signal from the vertical NPA (with neutral density and neutral attenuation corrections) and (*e*) the FIDA density. The more tangential left beams are injected from 1300 to 2750 ms, while an equal mixture of left and right beams are injected from 2750 to 4150 ms. The FIDA data are integrated over wavelengths between 649.6–650.8 and 661.3–662.6 nm for the channel that is centered at $R = 179.6$ cm. The dotted lines show the average values of the (*d*) NPA and (*e*) FIDA data over the four time periods: left beams and no ICH, left beams with ICH, mixed beams with ICH, mixed beams no ICH. $B_T = 1.53$ T; $I_p = 1.0$ MA.

$\rho \simeq 0.28$ prior to the sawtooth crash.) Despite this discrepancy, the enhancement in fast-ion pressure and density associated with RF acceleration is clearly seen by both diagnostics.

2.3. Database corroboration

To investigate systematic trends in the data, a database of all of the steady-state discharges in the 2005 campaign with both ICH power and FIDA data is compiled. For comparison purposes, many other discharges are included. This database of over 700 plasma conditions contains beam parameters (power, injection angle and energy), plasma parameters (electron density and temperature), flags that classify the low-frequency MHD activity and any Alfvénic activity in the 50–300 kHz frequency band, reduced data from the neutron, NPA, and FIDA diagnostics and many other quantities as well. For most entries, the data are averaged over 200–300 ms. In this paper, discharges with large tearing modes or appreciable Alfvénic activity are excluded.
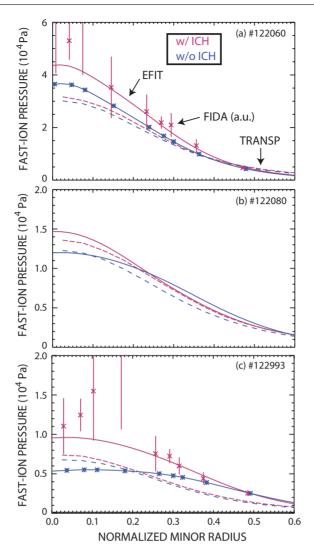
Figure 6. Fast-ion pressure inferred from equilibrium analysis (solid line) with and without ICH versus normalized minor radius ρ. (*a*) The fourth harmonic discharge shown in figure 3 at 2285 and 2065 ms. (*b*) A high-density fourth harmonic discharge at 4450 and 2670 ms. (*c*) The fifth harmonic discharge shown in figure 5 at 2445 and 1965 ms. The dashed lines are the fast-ion pressure predicted by TRANSP for classical behavior with ICH acceleration ignored. The symbols represent FIDA density data that are averaged over ~ 200 ms and $E_\lambda = 45$–75 keV; the data are normalized to agree with the pressure profile without ICH.

    When the 60 MHz ICH power exceeds 0.75 MW, the neutron rate usually exceeds the classical prediction (figure 7). Previous studies showed that a simple zero-dimensional model agrees well with the measured rate in quiet plasmas [34] but not in plasmas with strong Alfvénic activity [46], so this model is used here. For the present database, the neutron rate in discharges with ICH power > 0.75 MW is 50% larger than the discharges with < 0.75 MW of ICH power, confirming that fast-ion acceleration is generally observed.

    Figure 8 compares the neutron rate with the FIDA density for plasmas with various levels of 60 MHz ICH power. As expected in light of their similar sensitivity in velocity space (figure 2),
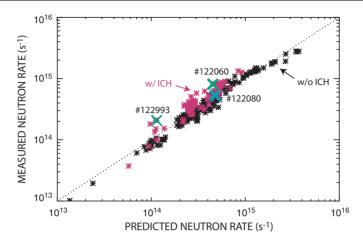
Figure 7. Measured neutron rate versus the prediction of a zero-dimensional model [34] for quiet plasmas with over 0.75 MW of ICH power (red) and with less than 0.5 MW of ICH (black). The three discharges selected for detailed analysis are indicated. None of the discharges have tearing or Alfven modes.
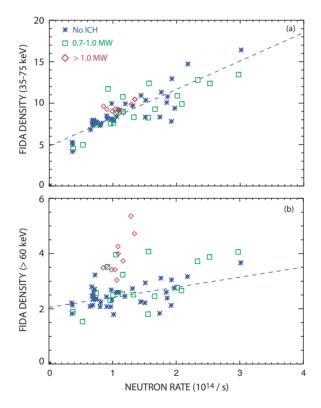

Figure 8. FIDA density at $R = 180$ cm averaged over E_λ of (a) 35–75 keV and (b) 60–90 keV versus the neutron rate for 60 MHz ICH power above 1.0 MW ($\Diamond$), between 0.7–1.0 MW ($\square$) and without ICH (*). The dashed lines are linear fits to the data in the absence of ICH. $B_T > 1.9$ T; only left beams.
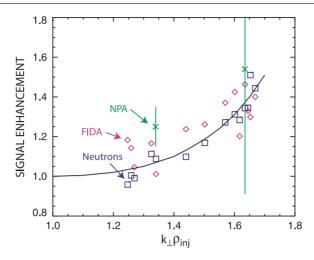
Figure 9. Signal enhancement during ICH for the neutron (□), FIDA (◇), and NPA (x) diagnostics versus the normalized gyroradius of the injected beam ions for all of the fourth harmonic discharges with quiet MHD and > 0.5 MW of 60 MHz ICH in the database. The abscissa employs the approximation $k_\perp \simeq \omega_{RF}/v_A$, with the Alfvén speed evaluated using the line averaged electron density and nominal toroidal field. The solid curve is taken from [11]. The FIDA data are from the $R = 180$ cm channel and are averaged over $E_\lambda = 55$–80 keV. The NPA points are the mean and standard deviation of several discharges with the analyser set to measure neutrals of 50 keV.

the neutron rate correlates well with the FIDA density for values of E_λ that correspond with the bulk of the distribution function (figure 8(*a*)). Note that, although a 'tail' above the injection energy is clearly evident in the velocity spectra (e.g. figure 4), the total number of particles above the injection energy is relatively small, so the bulk FIDA density ($E_\lambda > 35$ keV) still correlates well with the neutron rate even when the velocity distribution is distorted. This is not true above the injection energy, however. For large values of E_λ, discharges with over 1.0 MW of ICH power invariably have larger high-energy signals than predicted by the usual (no-ICH) scaling, while discharges with 0.7–1.0 MW occasionally contain a tail (figure 8(*b*)).

In a previous study [11], the enhancement of the neutron rate over the classically expected level showed good agreement with a simple model of the fourth harmonic acceleration that depends on the parameter $k_\perp \rho_f$. Here ρ_f is the fast-ion gyroradius at the injection energy and angle and $k_\perp$ is estimated from the Alfvén speed v_A and the wave frequency ω_{RF}, $k_\perp = \omega_{RF}/v_A$. As shown in figure 9, the neutron data from the 2005 discharges also agree well with this simple model. Note that the neutron rate performs an effective average over the fast-ion distribution function in both velocity and configuration space. The FIDA diagnostic also averages over much of velocity space (figure 2) but is localized in configuration space. For the database, the FIDA density correlates nearly as well with $k_\perp \rho_f$ as the neutron enhancement (correlation coefficients of $r = 0.82$ and $r = 0.95$, respectively) (figure 9). In contrast, the NPA diagnostic is highly localized in both velocity and configuration space and shows virtually no correlation with $k_\perp \rho_f$ ($r = 0.02$ for the six measurements represented by the symbols in figure 9).

3. Comparison with theory

The CQL3D code [31] solves the Fokker–Planck equation for the fast-ion distribution function. In the version of the code employed here, the wave fields in the quasilinear RF operator
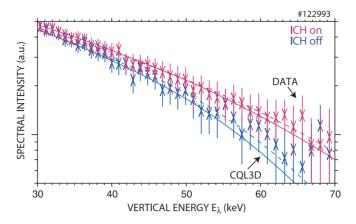
Figure 10. Measured (symbols) and calculated (curves) FIDA spectra with (2200–2700 ms) and without (1500–2000 ms) ICH in the fifth-harmonic discharge shown in figure 5. The CQL3D predictions are for the 180 cm channel (——) and for the 176 cm channel (- - - -); the data are from the 180 cm channel.

Q are found using ray tracing (for the antenna parameters in [11]). The code treats the fast-ion orbits in a zero banana-width approximation and is run for several slowing-down times to obtain a steady-state distribution function with and without RF. The calculated distribution function prior to ICH resembles the TRANSP prediction but is smoother (due to the absence of Monte Carlo noise) and is slightly narrower in pitch (due to the neglect of finite-orbit and charge-exchange effects). To compare with the FIDA data, the distribution functions are mapped into the coordinates used in the FIDA simulation code [28, 43], namely $F(E, p, x, y, z)$, where (x, y, z) are Cartesian coordinates along the neutral beam that produces the FIDA signal. The FIDA simulation code uses F and the computed injected and halo neutral densities in a weighted Monte Carlo scheme to predict the spectral intensity for the nine FIDA channels. For the classical distribution function calculated by TRANSP, this procedure gives good agreement with the measured intensity and spectral shape in quiet plasmas [43].

The analysed case is the fifth-harmonic acceleration discharge of figure 5 (#122993). One check of the CQL3D simulation is to compare the enhancement in the neutron rate during ICH with the measured value. The predicted enhancement is 1.8, while the measured value is 2.2.

The simulated FIDA spectra are similar to the measurements (figure 10) both before ICH and during ICH. Near the injection energy, both the data and the simulation increase by $\sim 50\%$ during ICH. (Recall from figure 2 that the signal at $E_\lambda \simeq 50$ keV originates primarily from ions with $E \simeq 80$ keV.) The measured spectral shape during ICH is in excellent quantitative agreement with the CQL3D prediction: the reduced chi-squared over the energy range $E_\lambda = 40$–70 keV is $\tilde{\chi}^2 = 0.13$. The agreement is even better if the simulated spectra from a channel 4 cm closer to the resonance layer is selected. As discussed below, because it uses a zero-banana width model, CQL3D predicts that the maximum acceleration occurs closer to the resonance layer than observed experimentally.

In order to determine the radial position of the fast-ion acceleration, figure 11 shows the enhancement of the FIDA density as a function of major radius. For the fifth-harmonic discharge, the profile peaks about 10 cm farther out in radius than the nominal fifth-harmonic resonance layer. The shift is similar for central fourth-harmonic heating: an average outshift
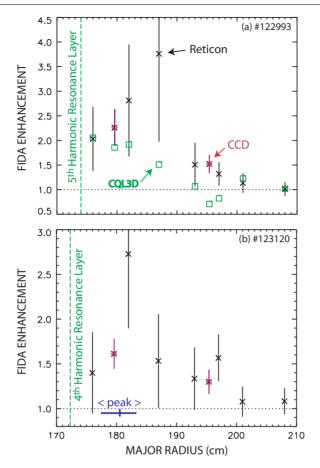
Figure 11. Relative change in FIDA density during ICH versus major radius for central (*a*) fifth harmonic heating and (*b*) fourth harmonic heating. The data from the dedicated diagnostic (∗) are integrated over $E_\lambda = 48\text{--}77\,\text{keV}$ and the data from the diagnostic that uses Reticon detectors (x) are integrated over wavelengths that correspond to $E_\lambda = 45\text{--}65\,\text{keV}$. The square symbols are the theoretical predictions of the CQL3D code. The dashed lines represent the nominal resonance layer without fast-wave Doppler shift corrections. In the lower figure, the average and standard deviation of the peak location for five discharges similar to #123120 are indicated by the symbol near 180 cm.

of 8 cm is observed (figure 11(*b*)). In earlier work [10], the enhancement in the neutron rate was maximized when the magnetic axis was ∼ 5 cm outside of the nominal resonance layer; this shift is consistent with the expected $k_\phi v_\phi$ fast-wave Doppler shift, where k_ϕ is the vacuum toroidal wavenumber and v_ϕ is the toroidal velocity of the injected beam ions. Empirically, the peak in the FIDA spectrum is a few centimeters farther out than this.

CQL3D predicts a slightly smaller outshift than observed experimentally (figure 11(*a*)). The likely explanation for this discrepancy is the zero-banana width approximation in CQL3D. Figure 12 shows a collection of particle orbits that have the correct value of vertical velocity to contribute to the observed spectral enhancement at the major radius of maximum FIDA enhancement. These orbits have turning points that are in good agreement with the expected resonance layer (including $k_\phi v_\phi$ fast-wave Doppler shift). In general, because of the nature of banana orbits, accelerated fast ions with turning points at the resonance layer must have an
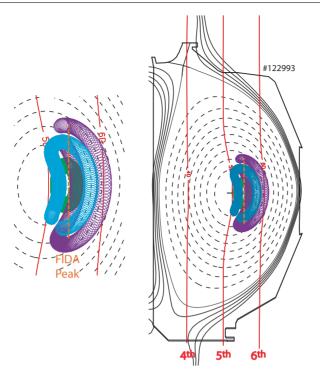
Figure 12. Elevation of DIII-D for the discharge shown in figure 5, showing the projection of representative orbits that have values of v_z that contribute strongly to the observed enhancement of the FIDA signal and are launched from the radial location of the peak of the FIDA enhancement. The dashed lines represent flux surfaces and the solid lines represent the nominal resonance layers (neglecting Doppler shifts).

average major radius $\langle R \rangle$ that exceeds the resonance layer. This simple orbital effect appears to account for the outward shift of the FIDA spatial profile.

4. Conclusion

Balmer-alpha spectroscopy is a powerful technique for the diagnosis of ion cyclotron acceleration of hydrogenic fast ions. The spectrum is sensitive to the distortion of the velocity distribution. The spatial profile depends on the wave absorption by the fast ions. The FIDA data are consistent with independent neutron and fast-ion pressure profile measurements.

The various fast-ion diagnostics are complementary. General trends, such as the dependence of fast-ion acceleration on $k_\perp \rho_f$, are most apparent in a diagnostic (like the neutron rate) that effectively integrates over all of phase space. For spatial density profiles, effective integration over velocity space (as in the FIDA and p_f techniques) is helpful. On the other hand, for detailed information about which portion of velocity space interacts with the waves, local measurements in velocity space by a NPA or similar diagnostic are best.

In light of its zero-banana width model, the CQL3D simulation is in reasonable agreement with the FIDA data. Comparison with the finite banana-width treatment implemented in ORBIT-RF [47] is in progress. In future work, the combination of temporal, spectral and spatial resolution should allow for stringent tests of theoretical models of wave absorption.

A planned experiment will investigate the role of the accelerated fast-ion population in the stabilization and destabilization of 'monster' sawteeth.

Appendix. Formulas for diagnostic weight functions and error bars

The velocity-space weight function $W(E, p)$ for the FIDA diagnostic depends on three factors: the minimum energy, the gyroangle weighting and the probability of a charge-exchange reaction.

The minimum energy that produces a particular Doppler shift was previously discussed for the special case of a perpendicular view [30]. Here, we generalize the expression given there to arbitrary viewing geometry. Consult figure 1 of [30] for an illustration of the geometry of gyromotion and its impact on the measured wavelength. The unit vector from the measurement volume to the collection lens is $\hat{\lambda}$. Decompose this unit vector into components parallel and perpendicular to the magnetic field, $\hat{\lambda} = \lambda_\parallel \hat{b}_\parallel + \lambda_\perp \hat{b}_{\perp 1}$, where $\hat{b}_\parallel$ is a unit vector parallel to $\vec{B}$ and $\hat{b}_{\perp 1}$ is the unit vector perpendicular to $\vec{B}$ that is in the same plane as the sightline and $\hat{b}_\parallel$. (The third unit vector, $\hat{b}_{\perp 2}$ is perpendicular to this plane.) The fast ion has a velocity $\vec{v}$. Its velocity component along $\hat{\lambda}$ determines the Doppler shift $\Delta\lambda$, $(\hat{\lambda} \cdot \vec{v})/c = \Delta\lambda/\lambda_0$. ($\lambda_0$ is the unshifted wavelength and c is the speed of light.) The Doppler-shift velocity component is $\hat{\lambda} \cdot \vec{v} = \lambda_\parallel v_\parallel + \lambda_\perp v_{\perp 1}$. Here, $v_{\perp 1}$ is the component of the perpendicular velocity $\vec{v}_\perp$ that is along $\hat{b}_{\perp 1}$; this component rapidly changes because of the particle gyromotion. Straightforward algebra yields the minimum energy E of a fast ion that can produce a Doppler shift that corresponds to an energy E_λ,

$$E = \frac{E_\lambda}{(\lambda_\parallel p + \lambda_\perp \sqrt{1 - p^2})^2}, \tag{1}$$

where p is the fast-ion pitch $v_\parallel/v$. Note that for $\lambda_\parallel = 0$, $\lambda_\perp = 1$, this reduces to equation (2) of [30]. In (E, p) space, all particles to the left of the curve described by equation (1) have $W = 0$.

The minimum energy that can produce a given Doppler shift (equation (1)) occurs when the perpendicular component of the fast-ion velocity is either parallel or anti-parallel to $\hat{b}_{\perp 1}$. For other values of the gyroangle φ, higher energy is needed to produce the observed Doppler shift. In terms of gyroangle, the fast-ion velocity component along $\hat{b}_{\perp 1}$ is $v_\perp \cos\varphi$. In the region of velocity space with sufficient energy to contribute to E_λ, the gyroangle of the fast ions that contribute is

$$\varphi = \cos^{-1}\left\{\frac{\pm\sqrt{E_\lambda/E} - \lambda_\parallel p}{\lambda_\perp \sqrt{1 - p^2}}\right\}, \tag{2}$$

where the $+(-)$ sign is for a blue(red)-shifted photon. Since the gyromotion is uniform, all values of gyroangle are equally likely. However, since the velocity component along $\hat{b}_{\perp 1}$ is proportional to $\cos\varphi$, the relative contribution to the spectrum is greatest for ions with φ near zero or π, where the velocity component changes slowly. ('Wings' at maximal Doppler shifts is a familiar spectral feature produced by gyrating, monoenergetic particles; see, e.g. [48].) To derive the weight function associated with gyromotion, note that

$$\int_{\lambda_{min}}^{\lambda} W_\varphi(\lambda) \, d\lambda \propto \int_0^\varphi g(\varphi) \, d\varphi. \tag{3}$$

Here $g(\varphi)$ is the probability of finding the fast ion at a particular gyroangle, which is $g(\varphi) = 1/(2\pi)$ for uniform gyromotion. Differentiate equation (3) and use equation (2)

to obtain the gyroangle weight function,

$$W_\varphi \propto (\sqrt{E}\sqrt{1-p^2}\sin\varphi)^{-1}. \tag{4}$$

Although equation (4) is a useful analytical description of W_φ, it is inconvenient for numerical work because it is singular at $\varphi = 0$. For numerical work, it is more convenient to calculate the fraction of particles that contribute to a particular energy bin of width δE_λ. The weight function W_φ is proportional to the range of gyroangles that can contribute to this energy bin, $W_\varphi \propto |\varphi_{max} - \varphi_{min}|$. The range of gyroangles is readily calculated using equation (2).

The final factor that contributes to the FIDA weight function is the probability of a charge-exchange reaction that converts a fast ion into a neutral in the $n = 3$ energy level, W_{cx}. This factor depends upon the relative velocity between the particular fast ion under consideration and all of the neutral populations associated with the diagnostic beam (full, half, and third energy components and the halo-neutral population). In addition, a full treatment must consider the energy-occupation levels of the various neutral populations and the cross section from each energy level to the $n = 3$ level. For a given point in (E, p) space, the gyroangles that can contribute to a specified E_λ are given by equation (2), so the relative velocity is readily determined for use in evaluation of the reactivities σv. For simplicity, halo neutrals and reactions from excited energy levels are neglected in the calculation of W_{cx} shown in figure 2. The total FIDA weight function is the product of W_φ and W_{cx}.

The weight function for the p_f measurement is

$$W_{pres} \propto E(p^2 + \sqrt{1-p^2}/2). \tag{5}$$

The weight function for beam-plasma neutron measurements depends on the relative velocity of the fast ions with the thermal deuterons. We assume that the distribution for the thermal deuterium is described by a drifted Maxwellian with temperature T_i and drift velocity v_{rot} in the $\hat{b}_\parallel$ direction. $W_{neutron}$ is found by integrating the d–d reactivity σv over the thermal distribution function with (E, p) specified.

The dominant errors in the FIDA measurements are the uncertainties associated with background subtraction. When the FIDA 'density' is shown, the uncertainty in calculation of the injected neutral density contributes additional uncertainty. The error associated with background subtraction is readily calculated. The FIDA signal $S = T - B$, where T is the total signal and B is the background. An ensemble of N_T measurements of T are obtained when the diagnostic beam is on; these data have mean $\langle T \rangle$ and standard deviation σ_T. Similarly an ensemble of N_B measurements of B are obtained when the beam is off that have mean $\langle B \rangle$ and standard deviation σ_B. The FIDA signal is $\langle T \rangle - \langle B \rangle$ and the one-sigma error is $\sigma = \sqrt{\sigma_T^2 + \sigma_B^2}$. For the FIDA 'density,' this uncertainty is added in quadrature with the estimated error in the injected neutral density (typically 10%).

The FIDA relative profile measurements depend on six quantities: T_1, B_1, T_2, B_2, n_1 and n_2, where the subscripts represent the first and second time intervals for the measurements (with and without ICH) and n_1 and n_2 are the injected neutral densities. The relative signal is $S = (n_2/n_1)(\langle T_1 \rangle - \langle B_1 \rangle)/(\langle T_2 \rangle - \langle B_2 \rangle)$. The fractional uncertainty due to the background subtraction is

$$\frac{\sigma}{S} = \left[\frac{\sigma_{T1}^2 + \sigma_{B1}^2}{(\langle T_1 \rangle - \langle B_1 \rangle)^2} + \frac{\sigma_{T2}^2 + \sigma_{B2}^2}{(\langle T_2 \rangle - \langle B_2 \rangle)^2} \right]^{1/2}. \tag{6}$$

The uncertainty in the relative injected neutral density adds in quadrature, as before.

With the assumption that the carbon and deuterium temperatures are both T_i and that the plasma is quasineutral with carbon the dominant impurity, the fast-ion pressure p_f is

$$p_f = p - n_e T_e - (n_e - 6n_C)T_i - n_C T_i, \tag{7}$$

where p is the total pressure from EFIT and n_C is the carbon density. The uncertainty in fast-ion pressure δp_f is

$$\delta p_f = [(\delta p)^2 + (T_e + T_i)^2 (\delta n_e)^2 + n_e^2 (\delta T_e^2 + \delta T_i^2) + 25 n_C^2 \delta T_i^2 + 25 T_i^2 \delta n_C^2]^{1/2}. \qquad (8)$$

The terms involving δp and δn_e are usually dominant.

Acknowledgments

References

[1] Biddle A P and Sprott J C 1981 *Plasma Phys.* **23** 679
[2] Seki T *et al* 1991 *Nucl. Fusion* **31** 1369
[3] Sadler G *et al* 1992 *Plasma Phys. Control. Fusion* **34** 1971
[4] Van Wassenhove G *et al* 1992 *Proc. EPS Topical Conf. on RF Heating and Current Drive of Fusion Devices (Brussels)* p 141
[5] Kimura H *et al* 1993 *Plasma Phys. Control. Fusion* **35** 845
[6] Koch R *et al* 1995 *Plasma Phys. Control. Fusion* **37** A291
[7] Nemoto M *et al* 1997 *Plasma Phys. Control. Fusion* **39** 1599
[8] Petty C C *et al* 1997 Fast wave current drive in neutral beam heated plasmas on DIII-D *Proc. 12th Int. Conf. on Radio Frequency Power in Plasmas (Savannah, 1997)* (New York: AIP) p 225
[9] Eriksson L-G *et al* 1998 *Nucl. Fusion* **38** 265
[10] Pinsker R I *et al* Experiments on ion cyclotron damping at the deuterium fourth harmonic in DIII-D *Proc. 13th Int. Conf. on Radio Frequency Power in Plasmas (Annapolis, 1999)* (New York: AIP) p 144
[11] Heidbrink W W *et al* 1999 *Nucl. Fusion* **39** 1369
[12] Kusama Y *et al* 1999 *Plasma Phys. Control. Fusion* **41** 625
[13] Mantsinen M J *et al* 1999 *Plasma Phys. Control. Fusion* **41** 843
[14] Petty C C *et al* 2001 *Plasma Phys. Control. Fusion* **43** 1747
[15] Mantsinen M J *et al* 2002 *Phys. Rev. Lett.* **88** 105002
[16] Noterdaeme J-M *et al* 2003 *Nucl. Fusion* **43** 202
[17] Rosenberg A L *et al* 2004 *Phys. Plasma* **11** 2441
[18] Ivanov N V, Kovan I A and Sokolov Y A 1976 *Sov. Phys.-JETP* **24** 316
[19] Heidbrink W W and Sadler G J 1994 *Nucl. Fusion* **34** 535
[20] Chrien R E *et al* 1981 *Phys. Rev. Lett.* **46** 535
[21] Cottrell G A and Start D F H 1991 *Nucl. Fusion* **31** 61
[22] Darrow D S *et al* 1996 *Nucl. Fusion* **36** 1
[23] Kiptily V G *et al* 2002 *Nucl. Fusion* **42** 999
[24] Kiptily V G *et al* 2005 *Nucl. Fusion* **45** L21
[25] Bindslev H *et al* 2006 *Phys. Rev. Lett.* **97** 205005
[26] Bernabei S *et al* 2000 *Phys. Rev. Lett.* **84** 1212
[27] Bernabei S *et al* 2001 *Nucl. Fusion* **41** 513
[28] Heidbrink W W, Burrell K H, Luo Y, Pablant N A and Ruskov E 2004 *Plasma Phys. Control. Fusion* **46** 1855
[29] Luo Y, Heidbrink W W and Burrell K H 2004 *Rev. Sci. Instrum.* **75** 3468
[30] Luo Y, Heidbrink W W, Burrell K H, Kaplan D H and Gohil P 2007 *Rev. Sci. Instrum.* **78** 033505
[31] Harvey R W and Mccoy M G 1992 *Proc. IAEA Technical Committee Meeting on Advances in Simulation and Modeling of Thermonuclear Plasmas (Montreal, 1992)* (Vienna: IAEA)
[32] Pinsker R I *et al* 2006 *Nucl. Fusion* **46** S416
[33] Gohil P, Burrell K H, Groebner R J and Seraydarian R P 1990 *Rev. Sci. Instrum.* **61** 2949
[34] Heidbrink W W, Taylor P L and Phillips J A 1997 *Rev. Sci. Instrum.* **68** 536
[35] Carolipio E M and Heidbrink W W 1997 *Rev. Sci. Instrum.* **68** 304
[36] Rice B W, Nilson D G, Burrell K H and Lao L L 1999 *Rev. Sci. Instrum.* **70** 815
[37] Lao L L, St John H, Stambaugh R D, Kellman A G and Pfeiffer W 1985 *Nucl. Fusion* **25** 1611

[38] Austin M E and Lohr J 2003 *Rev. Sci. Instrum.* **74** 1457
[39] Carlstrom T N *et al* 1992 *Rev. Sci. Instrum.* **63** 4901
[40] Carlstrom T N, Ahlgren D R and Crosbie J 1998 *Rev. Sci. Instrum.* **59** 1063
[41] Egedal J and Bindslev H 2004 *Phys. Plasma* **11** 2191
[42] Budny R V 1994 *Nucl. Fusion* **34** 1247
[43] Luo Y, Heidbrink W W, Ruskov E, Burrell K H and Solomon W M 2007 *Phys. Plasmas* **14** at press
[44] Campbell D J *et al* 1988 *Phys. Rev. Lett.* **60** 2148
[45] Philipona R *et al* 1990 *Rev. Sci. Instrum.* **61** 3007
[46] Heidbrink W W *et al* 1999 *Phys. Plasmas* **6** 1147
[47] Chan V S, Chiu S C and Omelchenko Y A 2002 *Phys. Plasmas* **9** 501
[48] Heidbrink W W 1984 *Nucl. Fusion* **24** 636